Oxidation Anisotropy and Size-Dependent Reaction Kinetics of Zinc Nanocrystals

Xiaofei Ma and Michael R. Zachariah*

Department of Mechanical Engineering and Department of Chemistry and Biochemistry, University of Maryland, College Park, Maryland 20742

Nanosized Zn and ZnO particles have attracted considerable interest for their various potential applications. Zn can act as both the fuel and a working catalyst in the Zn/ZnO thermochemical solar water splitting cycle for hydrogen generation, and ZnO is an important semiconductor. In this work, we combine two different ion-mobility schemes in series to study the size-resolved oxidation kinetics of zinc nanocrystals (NCs). The first mobility characterization size selects the NCs, whereas the second mobility characterization measures changes in mass resulting from a controlled oxidation of the NCs. A shrinking core model is used to extract the size-dependent oxidation activation energies, which are observed to be dependent on NC size. We also observed a strong anisotropy effect in the oxidation, as imaged by electron microscopy. An oxidation mechanism is proposed that qualitatively explains the oxidation anisotropy and its relationship to the surface energy of the Zn NCs.

Introduction

Zn is an attractive fuel and has been employed in powder form as a rocket propellant when mixed with sulfur.[1] Zinc is also used as the anode or fuel in the zinc−air fuel cell that forms the basis of the theorized zinc economy.[2] More recently, Zn/ZnO redox reactions have been considered for thermochemical two-step water-splitting cycles for hydrogen generation.[3−5] The cycle involves a Zn hydrolysis reaction to produce hydrogen, followed by the solar reduction of zinc oxide. In a recent study,[6] Zn nanoparticles have been employed so as to take advantage of their high surface-to-volume ratio and the ability to operate a continuous flow process.

As a wide band gap semiconductor, bulk ZnO has a band gap energy of 3.37 eV at room temperature and also exhibits piezoelectric properties. ZnO nanostructures, such as nanowires/belts, have attracted considerable attention because of their novel application in optical and electrical devices, sensors, and medical devices.[7−9] Although there exist many different techniques to prepare ZnO, the thermal oxidation from Zn is the most basic and is widely employed to create a variety of ZnO nanostructures.[10−14] Despite the widening application of Zn-based nanostructures, very little attention has been paid to the quantitative kinetics of Zn nanocrystal (NC) oxidation.
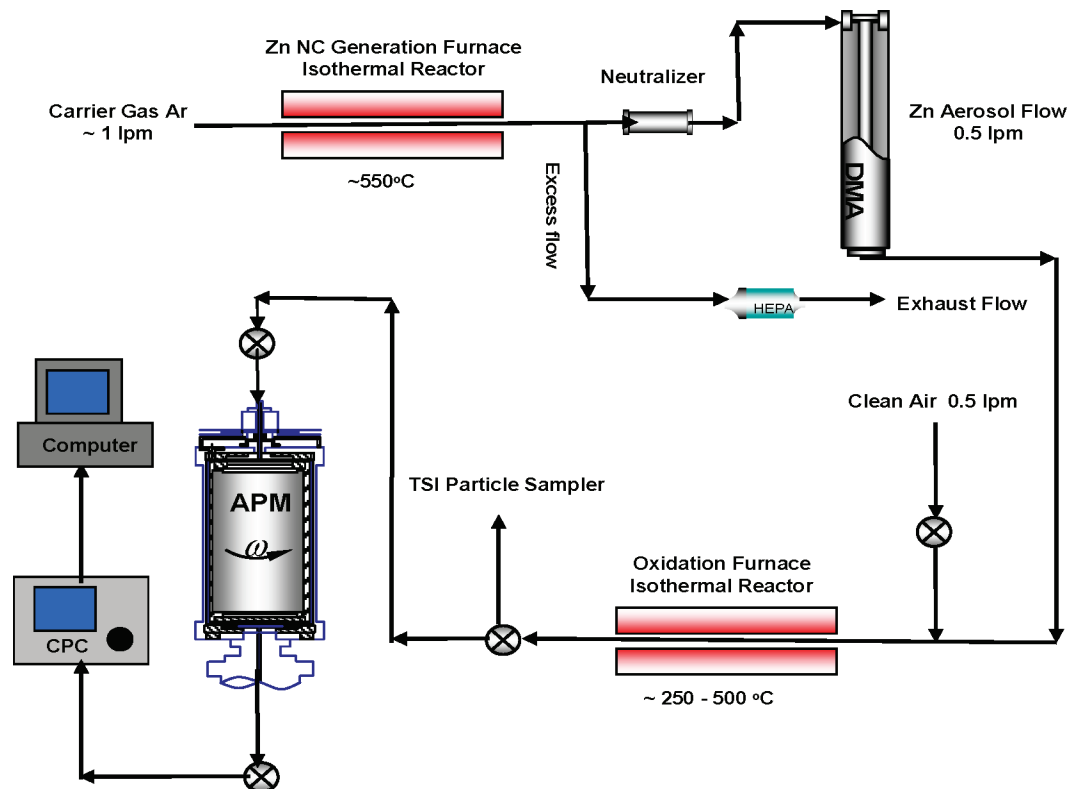
The general theory of metal oxidation and related transport phenomena in oxide films have been developed and studied for several decades. The theory proposed by Wagner is restricted to thick films.[15] His theory is based on two assumptions: electrical neutrality within the film and diffusion across the oxide film as the rate-liming step in the overall reaction. The theory leads to the parabolic growth law. However, the characteristic length (Debye−Huckel screening length) is on the order of several hundred nanometers to 1 μm.[16−18] Therefore, given the size of our Zn NCs (less than 100 nm), Wagner's theory does not apply. When the film thickness is less than 1 μm, the assumption of electrical neutrality is invalid, and when the film thickness is less than 20 nm, even the Nernst−Einstein relationship is unreliable.[16] Compared with a thick film, the

mechanism of thin film growth is not as well understood. There are a number of power laws that have been employed to describe the kinetics for the growth of thin films. The theory of Cabrera and Mott is useful when considering the growth mechanism of thin films.[19] In their theory, the thickening of the film is caused by the ionic transport across the film and the driving force is the electric field generated by electron transfer. However, the Cabrera and Mott theory contains parameters that cannot be measured independently, which makes it particularly difficult to apply in any quantitative analysis. It is believed that metal oxidation is a diffusion-controlled process. In this paper, the classic diffusion-controlled shrinking core model is applied in our study as a relatively straightforward way to extract reaction kinetics data of Zn NC oxidation.

An interesting phenomenon in solid crystal oxidation processes is that the oxidation rate is dependent on the crystal orientation. Some experiments have been conducted to investigate the crystal face dependence of the oxidation rate. For example, Liu studied millimeter sized single-crystal Ni surfaces using Auger electron spectroscopy (AES) and found the rate of oxygen uptake depended on crystal orientation {111}>{110}>{100}.[20] They proposed that packing of the absorbed oxygen on {111} surfaces is more compact and enhances the nucleation of bulk oxide. Munoz-Marquez[21] used medium-energy ion scattering (MEIS) to study the oxidation on Ni(100) and Ni(111) surfaces and found that oxide film growth proceeds significantly faster on Ni(111) than on Ni(100). However, no comparable studies have been conducted on free (unsupported) nanometer single crystals.

In this paper, we use electrical mobility classification and characterization to explore the size-resolved reactivity of Zn NCs in free flight and determine quantitative Arrhenius reaction parameters. We will also observe that oxidation is anisotropic, as imaged from electron microscopic analysis. What distinguishes this study from previous studies is first, free NCs are suspended in an inert gas environment, which means free of any potential substrate effects, and thus, all crystal planes are coexistent and exposed to the same experimental conditions simultaneously. Second, NCs are nanometer in size, which

---

* To whom correspondence should be addressed. E-mail: mrz@umd.edu.

Oxidation Anisotropy and Reaction Kinetics of Zn NCs

J. Phys. Chem. C, Vol. 113, No. 33, 2009 **14645**

Figure 1. Experimental system for Zn generation, size selection by DMA, oxidation, and subsequent mass analysis with the APM.

means there is a larger portion of atoms on the edges. Those edges are sharp interfaces between the crystal planes. Thus, edge effect may play an important role in the NC oxidation process.

Experimental Approach

The basic strategy for studying the reactivity of Zn NCs is to size select NCs and then quantify their size-resolved reactivity. The experimental system consists of three components: preparation of monodisperse Zn NCs, exposure of size-selected Zn NCs into a controlled temperature region, and finally, measurement of the mass change resulting from oxidation. A complete schematic of the experimental system with temperature and flow rate control is shown in Figure 1. Our experiment consists of two different ion-mobility schemes in series.[22] The first mobility characterization is to size select NCs with a differential mobility analyzer (DMA, homemade).[23-25] The second mobility characterization employs an aerosol particle mass analyzer (APM, model APM-3600, Kanomax Japan, Inc.)[26] and measures changes in mass resulting from a controlled oxidation of the Zn NCs.

Because we are employing ion-mobility methods, particles are first charged to a Boltzmann charge distribution by exposing the nanoparticle aerosol to a Po-210 source, before the DMA. The average charge state of sample particles under Boltzmann distribution is quasi-neutral, with most of the particles uncharged and equal amounts of particles carry ± 1 charge and ±2 charges, etc. For example, in the case of 50 nm particles, 60.2% of the particles will be neutral, 19.3% carry ±1 charge, 0.6% carry ± 2 charges, and a higher charge state would be even less. Considering the small percentage in the multiple charged states, we ignore multiple charged particles. Both the DMA and the APM are configured to classify positively charged particles for these experiments.

1. In Situ Generation of Monodisperse Zn NCs. The Zn NCs are generated using an evaporation/condensation method

in argon. Granular Zn (purity, 99.99% from Sigma-Aldrich) contained in a small ceramic boat was placed in a tube furnace at 550 °C to generate a flow of Zn vapor. The Zn vapor condenses as it exits the tube furnace, and by empirical adjustment of the tube furnace temperature and the argon carrier gas flow rate, we were able to form unagglomerated Zn NCs. Because our objective is to study size-resolved reactivity, we use a DMA as a band-pass filter to generate monodisperse NCs. The DMA selects particles based on their electric mobility, which is related to the drag force and charge on a particle. For particles of the size being considered here, the particles are being selected based on their projected surface area.[23,27,28]

2. DMA−APM System. The DMA, used in this experiment for generating monodisperse NCs, consists of an annular region between two concentric cylinders, with the center cylinder held at high voltage and the outer one at ground. Charged particles of the right polarity feel an attractive force toward the center electrode and move radically inward at a constant electrophoretic velocity, determined by the particle charge and drag force (which is a function of particle size). When charged particles flow between the cylinders, the electric force on the particle is balanced by the drag force, and at a fixed voltage, all particles exiting the instrument have (to the resolution of the instrument) equivalent mobility sizes. In the size range of consideration here, the DMA functions as a source of mono-area NCs.

The APM can determine the particle mass distribution based on the particle mass to charge ratio and is used in our experiment to monitor changes to the particle mass resulting from oxidation. The APM consists of two concentric cylindrical electrodes that rotate together at a controlled speed. An electric field is created by applying high voltage on the inner electrode, while the outer one is held at ground. Charged particles flowing within the concentric cylinders experience opposing centrifugal and electrostatic forces, and as a result, particles exiting the instrument (for fixed voltage and rotation speed) all have the same nominal

mass. By scanning either the voltage or the rotation speed, one can determine the particle mass distribution (independent of particle shape). APM mass measurements are independent of particle morphology because the centrifugal force is directly proportional to the mass. Our previous experiments have used the DMA−APM technique to measure the inherent density of nanoparticles, as well as to study the mechanism of aluminum and nickel oxidation.[22,29]

On the basis of the operating conditions for the DMA and APM, we estimate uncertainties as follows. For the DMA, the uncertainty is based on the theoretical transfer function that will give an uncertainly in the peak particle size of ± 4%. We then use a Gaussian fit to determine the peak size, which would have a precision uncertainty of no more than 1%. A similar result can be obtained for the APM; however, the uncertainties are not due to the transfer function but uncertainties in the step voltage that has a resolution of only ± 0.5 V, which gives an uncertainty in mass of ∼4%. Using the root-sum-square (RSS) method, we can estimate the uncertainty in density to be ∼5%. This is consistent with our prior work using combined DMA/APM on reference aerosols (NaCl and DOP), which gave an experimentally determined uncertainly in density of 4%. Furthermore, our DMA/APM mass measurements of NIST SRM 60 and 100 PSL spheres were within about 1.4% and 5.6%, respectively (Lall et al., 2009).[37]

**3. Zinc NC Characterization, Sampling, and Oxidation.** In our experiment, Zn NCs of initial ion-mobility sizes of 50, 70, and 100 nm were selected in sequential experiments to study the size-dependent oxidation. After size classification, the Zn aerosol flow is mixed with air at the ratio of 1:1 and then passes through a second tubular reactor. This flow tube reactor enables the controlled oxidation of the Zn NCs for residence times of 2−4 s. The total flow rate of the aerosol flow is 1 liter per minute at standard condition. To monitor the small mass change of the NCs due to oxidation, an aerosol particle mass analyzer (APM) is placed downstream. Particles exiting the APM will be selected on the basis of mass and are counted using standard particle counting methods using a condensation particle counter (CPC).

In the experiment, the temperature in the oxidation furnace was set between 250 °C and 500 °C in increments of 25 °C. The particle mass distribution was then measured for each reactor temperature after the system reached steady state. The room-temperature particle mass distribution was also taken and set as the base of the mass measurement. Samples for electron microscopic analysis were collected exiting the evaporation furnace by electrostatically precipitating the aerosol onto a TEM grid.

Results and Discussion

1. Zn NC Morphology. Figure 2 shows the SEM image of two single Zn NCs that were deposited from the gas phase by electrostatic precipitation to a TEM grid. The NCs so obtained show a perfect hexagonal prism. Energy dispersive X-ray (EDS) spectra obtained from the NCs in SEM confirmed that the composition is Zn. The crystal structure of zinc is hexagonal close-packed, which belongs to the space group *P*63/*mmc*. Selected-area electron diffraction analysis indicates that the Zn NCs have top surfaces of {0001} crystal planes and have side surfaces of {1$\bar{1}$00} planes.

2. Size-Dependent Reaction Rate. Figure 3 shows the normalized particle mass distributions for different initial sizes of Zn NCs oxidized in air at different temperatures, obtained from APM-CPC measurements. The particle number concentration is obtained as a 1 min time average of the CPC counts at
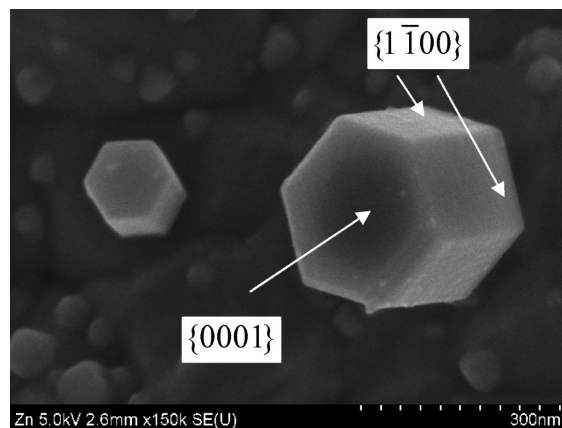
Figure 2. SEM image of the hexagonal-prism-shaped Zn NCs (before size selection).

each APM voltage. The peak mass of Zn NCs at each oxidation temperature is obtained by fitting the experimental data using a Gaussian distribution. The results in the figure show that the peak mass for each mobility size remains unchanged at low temperatures and then increases in mass at elevated temperatures, reflecting the increase rate of oxidation. Figure 4 shows the percentage conversion from Zn to ZnO as a function of reaction temperature for different sizes of NCs. As an example, for 50 nm Zn NCs, the oxidation starts at about 250 °C, and on the basis of the mass changes, we find that the NC has fully oxidized by ∼425 °C. Similar trends are observed for the other sizes of Zn NCs.
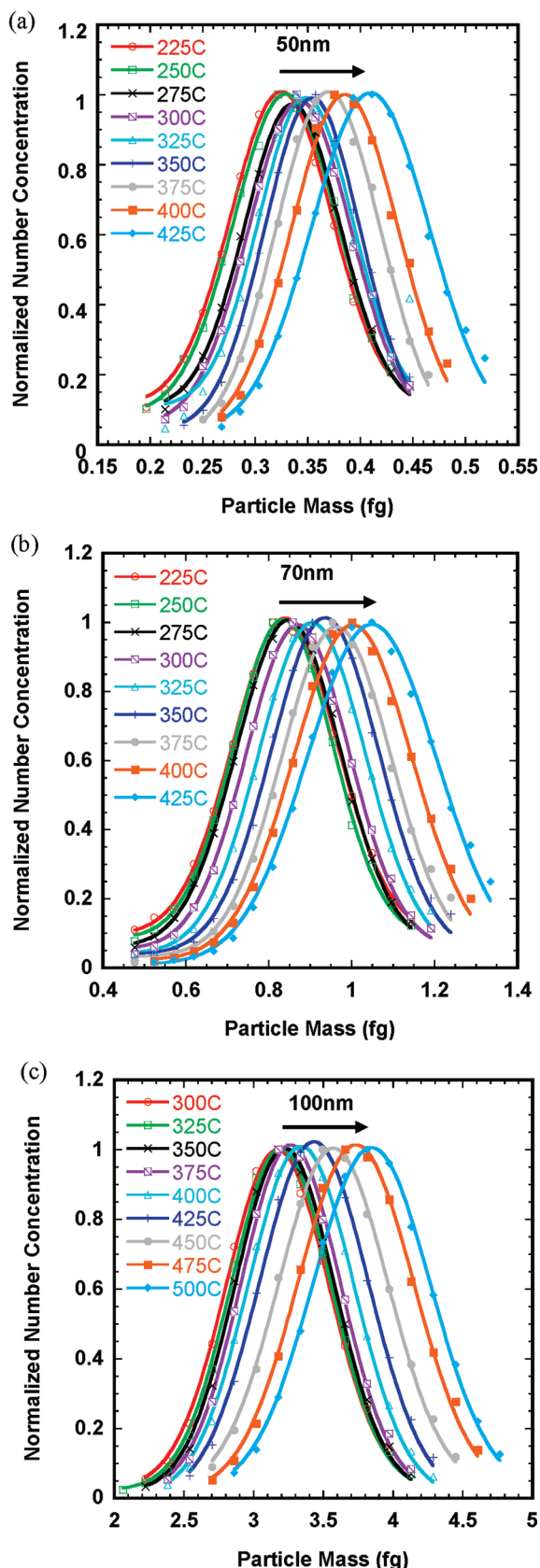
It is believed that metal oxidation is a diffusion-controlled process. This suggests that the classic diffusion-controlled shrinking core model could be applied in our study as a relatively straightforward way to extract reaction kinetics data.[30] The shrinking core model is typically described in three steps: (1) diffusion of gaseous reactant (oxygen) to the particle surface, (2) dissolution and diffusion of gaseous reactant (oxygen) through the oxide shell to the surface of the unreacted core, and (3) chemical reaction of the dissolved oxidizer with material (Zn) at the surface of the unreacted core. For spherical nanoparticles, Carter[31] applied the assumptions as in Wagner's theory to the shrinking core model and derived an oxidation rate law for metal particle oxidation. Following Carter's steady-state analysis, the diffusion flux through the oxide shell can be related to the reaction rate as

$$\frac{dN_{O_2}}{dt} = -4\pi D_e C_{O_2} \frac{r_c r_p}{r_p - r_c} \tag{1}$$

where N_{O_2} is the mole of oxygen in the oxide layer and C_{O_2} is the oxygen molar concentration in the gas phase. r_c and r_p are the radius of the zinc core and the reacted particle radius, respectively. D_e, the diffusion coefficient for ion diffusion in the oxide layer, is given by

$$D_e = A \exp\left(-\frac{E_a}{RT}\right) \tag{2}$$

where A is a size-dependent pre-exponential factor, E_a is the activation energy of the reaction, and R is the gas constant. Because the mass change of the reacted particle is due to

Oxidation Anisotropy and Reaction Kinetics of Zn NCs

J. Phys. Chem. C, Vol. 113, No. 33, 2009 **14647**

Figure 3. Normalized particle mass distributions for different mobility sizes of Zn NCs at different oxidation temperatures: (a) 50 nm, (b) 70 nm, and (c) 100 nm.

immediately obtained by substituting D_e in eq 1 using eq 2 where m is the absolute mass of the reacted particle and M_{O_2}

$$\frac{dm}{dt} = 4\pi M_{O_2} C_{O_2} D_e \frac{r_c r_p}{r_p - r_c} \tag{3}$$

is the molecular weight of oxygen. Knowing the furnace temperature, the particle mass change Δm can be obtained by integrating eq 3 as the particles pass through the furnace. Considering the exponential temperature dependence of the rate constant and the fact that r_c and r_p are more temperature-dependent, we can approximate the instantaneous mass changing rate by the average mass changing rate $(\Delta m)/(\tau)$, where τ is the reaction time in the furnace. Thus, we can use the following equation to process our kinetic data:

$$\ln\left(\frac{\Delta m}{\tau}\right) = -E_a/RT + \ln\left(4\pi M_{O_2} C_{O_2} A \frac{r_c r_p}{r_p - r_c}\right) \tag{4}$$
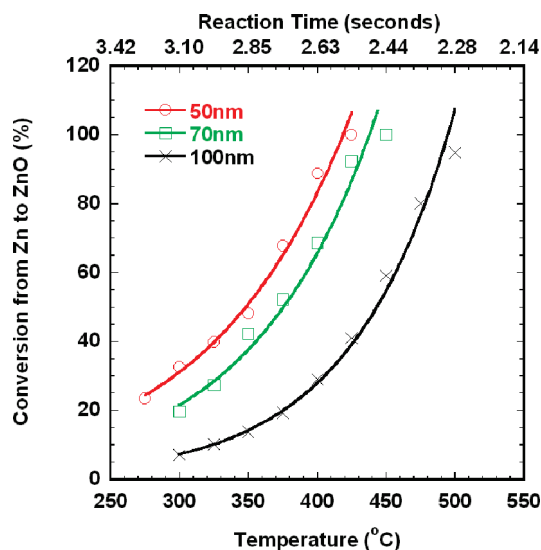
The reaction time at different furnace temperatures can be calculated using the following equation
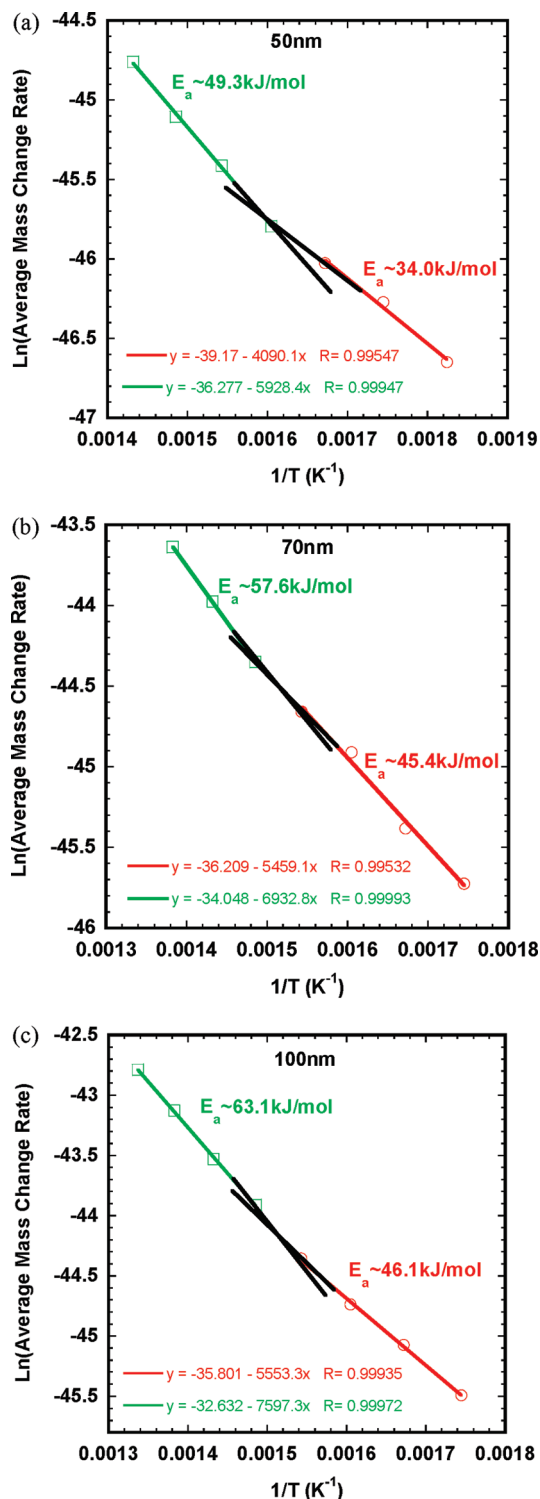
$$\tau = \int_0^L \frac{1}{u(x)} dx \tag{5}$$

where L is the length of the tube and $u(x)$ is the flow velocity, which can be calculated below as

$$u(x) = \frac{4}{3} u_m \frac{T(x)}{T_0} \tag{6}$$

where $(4/3)$ u_m is the peak flow velocity of carrier gas calculated from volume flow rate and the cross-sectional area of the flow tube under the assumption of laminar flow. $T(x)$ is the temperature distribution within the tube at each furnace set point. On the basis of eq 4, the size-resolved activation energy can be obtained from an Arrhenius plot, as shown in Figure 5. Two different regimes of oxidation are represented by the two linear fits, represent a low temperature regime at lower temperatures,


Figure 4. Percentage of conversion from Zn to ZnO for different sizes of Zn NCs.

the addition of gaseous reactant (oxygen) to the particle, if we multiply both sides of eq 1 by the molecular weight of oxygen, the mass change rate of the reacted particle can be

Figure 5. Arrhenius plot of reaction rates for different sizes of NCs: (a) 50 nm, (b) 70 nm, and (c) 100 nm.

followed by a faster oxidation regime occurring at higher temperatures. The intersection of the two straight lines represents the transition temperatures between the two regimes. For the case of the slower reaction, the activation energy decreases from 46.1 kJ/mol for 100 nm sized NCs to 34.0 kJ/mol for 50 nm NCs. For the high temperature regime, the activation energy decreases from 63.1 kJ/mol for 100 nm NCs to 49.3 kJ/mol for 50 nm NCs. In general, the smaller particles have a lower activation energy. We also conducted TGA experiments on a sample of commercial Zn nanoparticles. The sample with a mean
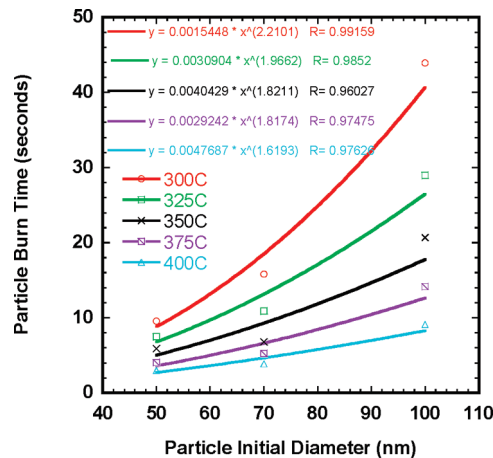

**Figure 6.** Particle burn time for different sizes of NCs at different reaction temperatures.

particle diameter of ~100 nm showed an activation energy of 128.7 kJ/mol, which is considerably higher than our experimental measurement and not unexpected. This difference between conventional methods and our approach has been consistently observed in previous studies.[32,33] It is well-known that bulk methods suffer from heat- and mass-transfer effects, where milligrams of an aggregated sample are needed, whereas the sample mass of our aerosol-based techniques is ~1 fg and is being determined on an isolated NC. Furthermore, for highly exothermic reactions, the reaction heat released will tend to exacerbate heat-transfer problems, whereas the DMA−APM techniques employed here allow for a direct measure of mass change of individual particles and thus enables us to explore the intrinsic reactivity of NCs while minimizing the sampling error introduced by mass and heat transfer. Because of the complexity of the rate expression, it is not easy to define a pre-exponential (A factor) in a simple Arrhenius form. Rather, we can say that the effective oxygen-sticking coefficient based on the oxygen flux and the mass change of the NC at different temperatures ranges from 1.0×10^{-7} to 1.0×10^{-6}.

Particle burn times for different sizes of NCs at different oxidation temperatures were also calculated based on the experimental reaction rate and the NC mass measured by the APM. Figure 6 plots the particle burn time as a function of particle size for various temperatures. In this case, the measurements are restricted to below the melting point. The particle burn time shows a size dependence close to $\sim D_p^2$, which is consistent with the oxide shell diffusion-controlled shrinking core model. However, the power of size dependence decreases slightly from 2.2 at 300 °C to 1.6 at 400 °C. This deviation may be partially explained by the slow and fast reactions for different sizes of NCs. For example, at a temperature of 350 °C, the oxidation of a 50 nm NC is in the fast reaction regime, while the 70 and 100 nm NCs are still in the slow reaction regime. Furthermore, this weaker size dependence (less than a power of two) has also been observed for Ni and Al oxidation.[22,29] On the basis of molecular dynamics simulation[34] on oxide-coated nanoparticles, the metal core is expected to have high internal pressures. A phenomenological model[29] developed for aluminum oxidation has shown that this higher internal pressure is at least partially responsible for a lower power dependence on particle size.

3. Zn NC Oxidation Anisotropy. To further explore the nature of the two oxidation regimes observed in the Arrhenius plots, samples of 100 nm Zn NCs were collected for electron microscopic analysis after oxidation at 350 °C, 400 °C, and 450
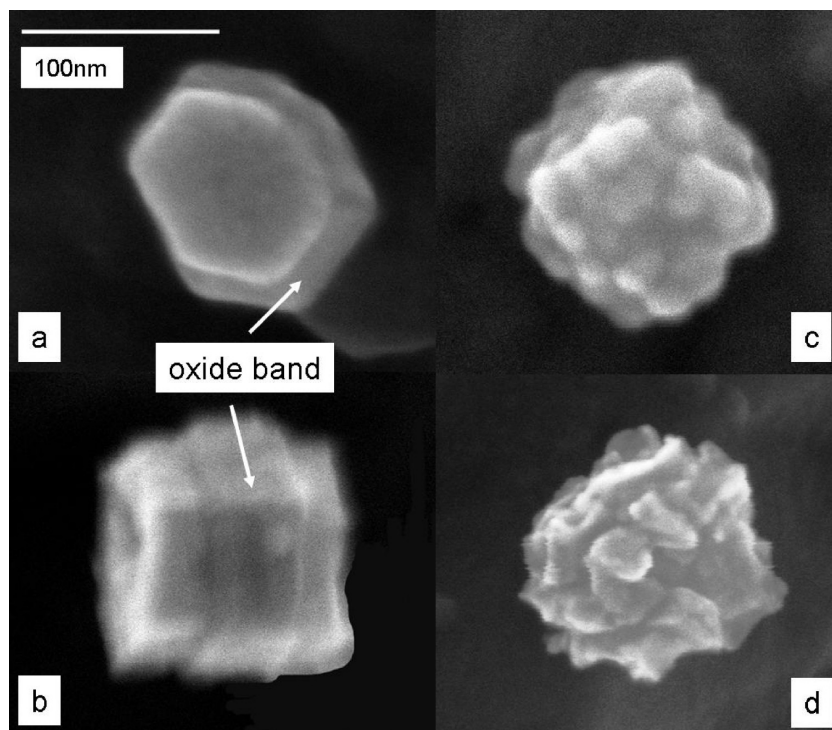
Figure 7. HR-SEM pictures of partially oxidized Zn NCs at different oxidation temperatures. (a) Top view of the NC at 350 °C. (b−d) Side view of the NC at 350 °C, 400 °C, and 450 °C, respectively.
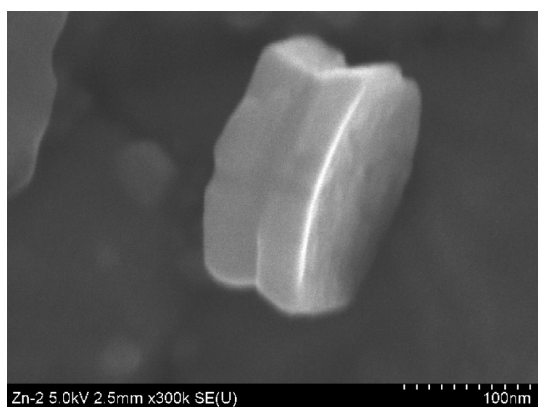
Figure 8. SEM image of a partially evaporated 100 nm Zn NC.

°C, which are below, close to, and above the transition temperature, respectively. The high-resolution SEM images are shown in Figure 7.

As we can see from the figure, there is a preferable surface of oxidation during the initial stages. From the images collected at 350 °C (Figure 7a,b), we see that there are band-shaped oxide layers formed around the six side surfaces of the NCs, whereas the top and bottom surfaces of NCs are flat and remain unchanged. The Zn NCs show a strong oxidation anisotropy with the rate of oxidation on Zn $\{1\bar{1}00\}$ planes much faster than that on the $\{0001\}$ planes. As the oxidation temperature increases to 400 °C, the Zn NC undergoes restructuring with the edges between the top surfaces and side surfaces becoming blurred. The NC deforms, and the original hexagonal prism shape cannot be distinguished. At oxidation temperatures well above the transition temperature (as shown in Arrhenius plots), the NC exhibits a flower-shaped morphology. Given the observed oxidation anisotropy, we propose the following reaction mechanism: at the lower oxidation temperatures, only the side surfaces of the NCs are activated and oxide layers are

formed first around those surfaces, whereas at higher oxidation temperatures, both the side and the top surfaces are activated, which enhances the oxidation kinetics but requires a higher activation energy. This, at least, is consistent with the observed kinetic regimes.

As discussed in the Introduction, our NCs are free of any potential substrate effects and there is a larger portion of atoms on the edges of our NCs. Those edges are sharp interfaces between the crystal planes. As such, evaporation and oxidation are taking place simultaneously from all faces, and thus, at the interface of these planes, either a morphology change with time or, alternatively a change in reaction rate must occur. No doubt these edge atoms are at a higher potential energy due to their lower coordination number and high strain and, thus, potentially more reactive. This, perhaps, is a more important distinction between millimeter sized crystals and NCs. We have observed an analogous anisotropy effect during the evaporation of Zn NCs in an inert atmosphere, which is the subject of another paper. Briefly, however, what we observed can be summarized in Figure 8, which shows a SEM picture of a partially evaporated 100 nm Zn NC. Most of the hexagonal-shaped top surfaces (Zn $\{0001\}$ planes) of the Zn NCs during evaporation are well-preserved relative to the side surfaces (Zn $\{1\bar{1}00\}$ planes). Material from the side surfaces is preferentially etched away, which leaves the side surfaces with a depression, while the top surfaces remain perfectly planar. Note that, in both evaporation and oxidation, it is the $\{1\bar{1}00\}$ that reacts preferentially. Furthermore, the reactivity is not homogeneous across the face but is most active away from the interface with the $\{0001\}$ surface. The behavior is consistent with the interface of the $\{0001\}$ surface acting as a pinning site. The evolving morphology is then a competition between the thermodynamic stability between the two planes and the reaction process.

Law[35] highlights this edge-enhanced oxidation effect in his ZnO nanowire growth mechanism. Furthermore, the side surfaces are Zn $\{1\bar{1}00\}$ planes that have a higher surface energy

than that of the top surfaces (Zn {0001} planes). It is known that high-energy surfaces tend to have an enhanced oxidation rate than that of low-energy surfaces, which are more stable.[36]

This oxidation anisotropy of NCs could, in principle, be applied to increase the reactivity of nanoenergetic materials or materials for solar thermal hydrogen generation, for example, by elongation of the *c* axis of NCs to maximize the high-energy surface area.

Conclusions

Size-classified substrate-free Zn NCs are explored for their oxidation kinetics using an in-flight tandem ion-mobility DMA−APM method. This method allows for a direct measure of the mass change of individual particles and thus enables us to explore the intrinsic reactivity of NCs while minimizing the sampling error introduced by mass and heat transfer occurring in traditional methods. Two reaction regimes were observed for Zn NC oxidation, a slower reaction regime at lower temperatures, followed by a faster oxidation regime occurring at higher temperatures. A shrinking core model is used to extract the size-dependent oxidation activation energies. Using electron microscopic analysis, we observed a strong effect of oxidation anisotropy. An oxidation mechanism based on surface energy anisotropy and edge-enhanced oxidation effects was proposed to explain the observed oxidation behavior of Zn NCs.

References and Notes

(1) Sutton, G. P. *Rocket Propulsion Elements*, 7th ed.; Wiley-Interscience: New York, 2000.

(2) Powering Future Vehicles with the Refuelable Zinc/Air Battery, Lawrence Livermore National Laboratory, *Science and Technology Review.* **October, 1995**.

(3) Steinfeld, A. *Int. J. Hydrogen Energy* **2002**, *27*, 611.

(4) Steinfeld, A. *Sol. Energy* **2005**, *78*, 603.

(5) Abu Hamed, T.; Davidson, J. H.; Stolzenburg, M. *J. Sol. Energy Eng.* **2008**, *130*, 041010.

(6) Ernst, F. O.; Tricoli, A.; Pratsinis, S. E.; Steinfeld, A. *AIChE J.* **2006**, *52*, 3297.

(7) Wong, E. M.; Searson, P. C. *Appl. Phys. Lett.* **1999**, *74*, 2939.

(8) Tang, Z. K.; Wong, G. K. L.; Yu, P.; Kawasaki, M.; Ohtomo, A.; Koinuma, H.; Segawa, Y. *Appl. Phys. Lett.* **1998**, *72*, 3270.

(9) Pan, Z. W.; Dai, Z. R.; Wang, Z. L. *Science* **2001**, *291*, 1947.

(10) Wang, Z.; Harris, R. *Mater. Charact.* **1993**, *30*, 155.

(11) Kim, S.; Jeong, M. C.; Oh, B. Y.; Lee, W.; Myoung, J. M. *J. Cryst. Growth* **2006**, *290*, 485.

(12) Wang, Y. G.; Lau, S. P.; Lee, H. W.; Yu, S. F.; Tay, B. K.; Zhang, X. H.; Hng, H. H. *J. Appl. Phys.* **2003**, *94*, 354.

(13) Lu, H. B.; Li, H.; Liao, L.; Tian, Y.; Shuai, M.; Li, J. C.; Fhu, M.; Fu, Q.; Zhu, B. P. *Nanotechnology* **2008**, *19*, 045605.

(14) Nakamura, R.; Lee, J. G.; Tokozakura, D.; Mori, H.; Nakajima, H. *Mater. Lett.* **2007**, *61*, 1060.

(15) Wagner, C. Z. *Z. Phys. Chem., Abt. B* **1933**, *21*, 25.

(16) Atkinson, A. *Rev. Mod. Phys.* **1985**, *57*, 437.

(17) Fromhold, A. T., Jr. *Theory of Metal Oxidation*; North Holland Publishing Company: Amsterdam, The Netherlands, 1976; Vol. 1.

(18) Fromhold, A. T., Jr. *Theory of Metal Oxidation*; North-Holland Publishing Company: Amsterdam, The Netherlands, 1980; Vol. 2.

(19) Cabrera, N.; Mott, N. F. *Rep. Prog. Phys.* **1948**, *12*, 163.

(20) Liu, H. T.; Armitage, A. F.; Woodruff, D. P. *Surf. Sci.* **1982**, *114*, 431.

(21) Munoz-Marquez, M. A.; Tanner, R. E.; Woodruff, D. P. *Surf. Sci.* **2004**, *565*, 1.

(22) Zhou, L.; Rai, A.; Piekiel, N.; Ma, X. F.; Zachariah, M. R. *J. Phys. Chem. C* **2008**, *112*, 16209.

(23) Liu, B. Y. H.; Pui, D. Y. H. *J. Colloid Interface Sci.* **1974**, *49*, 305.

(24) Liu, B. Y. H.; Pui, D. Y. H. *J. Colloid Interface Sci.* **1974**, *47*, 155.

(25) Knutson, E. O.; Whitby, K. T. *J. Colloid Interface Sci.* **1975**, *53*, 493.

(26) Ehara, K.; Hagwood, C.; Coakley, K. J. *J. Aerosol Sci.* **1996**, *27*, 217.

(27) Kim, S. H.; Woo, K. S.; Liu, B. Y. H.; Zachariah, M. R. *J. Colloid Interface Sci.* **2005**, *282*, 46.

(28) Jung, H. J.; Kittelson, D. B.; Zachariah, M. R. *Combust. Flame* **2004**, *136*, 445.

(29) Rai, A.; Park, K.; Zhou, L.; Zachariah, M. R. *Combust. Theory Modell.* **2006**, *10*, 843.

(30) Levenspiel, O. *Chemical Reaction Engineering*, 3rd ed.; John Wiley & Sons: New York, 1999.

(31) Carter, R. E. *J. Chem. Phys.* **1961**, *34*, 2010.

(32) Park, K.; Lee, D.; Rai, A.; Mukherjee, D.; Zachariah, M. R. *J. Phys. Chem. B* **2005**, *109*, 7290.

(33) Mahadevan, R.; Lee, D.; Sakurai, H.; Zachariah, M. R. *J. Phys. Chem. A* **2002**, *106*, 11083.

(34) Campbell, T.; Kalia, R. K.; Nakano, A.; Vashishta, P.; Ogata, S.; Rodgers, S. *Phys. Rev. Lett.* **1999**, *82*, 4866.

(35) Law, J. B. K.; Boothroyd, C. B.; Thong, J. T. L. *J. Cryst. Growth* **2008**, *310*, 2485.

(36) Gao, P. X.; Wang, Z. L. *J. Am. Chem. Soc.* **2003**, *125*, 11299.

(37) Lall, A. A.; Ma, X.; Guha, S.; Mulholland, G. W.; Zachariah, M. R. *Aerosol Science and Technology* **2009**, *43*, DOI: 10.1080/02786820903095484.